Article

Effect of K+ and Ca2+ Cations on Structural Manganese(IV) Oxide for the Aerobic Oxidation of 5-Hydroxymethylfurfural to 2,5-Furandicarboxylic Acid

Thinnaphat Poonsawat, Peerapong Promcharoen, Titiya Meechai,
Laksamee Chaicharoenwimolkul Chuaitammakit, and Ekasith Somsook*

Read Online

ACCESS | 📊 Metrics & More | 📖 Article Recommendations | 🆂🅸 Supporting Information

ABSTRACT: The promising influences of K+ and Ca2+ ions in the development of effective MnO_2 for the selective oxidation of 5-hydroxymethylfurfural to 2,5-furandicarboxylic acid (FDCA) were studied for the catalytic performance under a high-pressure reaction of aqueous O_2 (0.5 MPa) in a basic system. Various oxidation states of manganese in MnO_2 were able to accelerate the oxidation of 5-formyl-2-furancarboxylic acid to FDCA in the rate-determining step. The results were in good agreement that Ca2+ played a key role in the highest FDCA yield up to 85% due to the associated cations on the local coordination to enhance the high surface area and the electronic effect on the manganese ion. Both K−MnO_2 and Ca−MnO_2 catalysts showed excellent catalytic activities without a significant change in the efficiency in the reusability experiments.
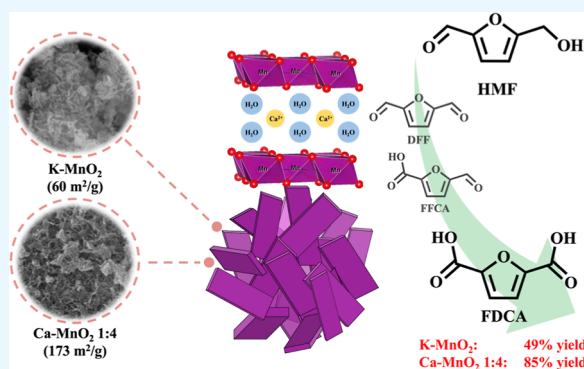
1. INTRODUCTION

Integrated biorefineries have been receiving more attention to increase the demand response in biogreen-circular economy for solving the environmental global issues leading to the sustainable development goals.[1−7] The technological foresight of 2,5-furandicarboxylic acid (FDCA), which is the superior performance properties of the bio-based chemical building block for polyethylene furanoate are focused on the market attractiveness to replace polyethylene terephthalate.[8−10] Particularly, 5-hydroxymethylfurfural (HMF) derived from cellulosic C6 sugars plays an important role in the chemical manufacture for the long-term investment to produce FDCA.[11−14] A feasibility study of stepwise reaction mechanism for HMF oxidation shown in Scheme 1 is proposed through two pathways, which include 5-hydroxylmethyl-2-furan carboxylic acid (HMFCA), 2,5-diformylfuran (DFF), and 5-formyl-2-furancarboxylic acid (FFCA) as intermediates.[15−18] In the past decade, various catalysts were investigated for the significant reactivity in the oxidation of HMF to yield FDCA at the high temperature and pressure.[19,20] The historical FDCA production was conducted in the oxidation process of HMF by electrochemical oxidation,[21,22] biocatalysts,[23,24] heterogeneous catalysts,[25−27] homogeneous catalysts,[28,29] and photocatalysts[30−32] as well as the process without any catalyst. The utilization of homo- and heterogeneous catalysts is still promising for practical applications. The limitation of the FDCA production from HMF at a large scale has been more considered in terms of the thermal stability of HMF in harsh

condition during the oxidation process to produce unidentified byproducts called humins.[33] In the current research regime of FDCA production, heterogeneous catalysts have been more attractively developed due to the stability and reusability. The oxidative catalytic methods have been extensively studied in various process of noble metals [gold (Au),[34,35] palladium (Pd),[36] platinum (Pt),[37] rhodium (Rh),[38] and ruthenium (Ru)[39] and non-noble metals [cerium (Ce),[40] cobalt (Co),[41] iron (Fe),[42] and manganese (Mn)[43−45] supported heterogeneous catalysts. Moreover, the nonbase oxidation of HMF was studied over the Co−Mn−Br catalysts to produce high yield of FDCA.[46−49] Interestingly, a promising nonprecious manganese oxide (MnO_2) could act as an effective heterogeneous catalysts for the aerobic oxidation of HMF to FDCA in which the catalytic performance was determined by the oxygen vacancy formation.[50,51] Recently, calcium manganese oxide has been taken as an inspiration to achieve the goals of biomimetic oxygen-evolving catalysts and organic sulfide oxidation.[52−54] Although the calcium manganese oxides have been used to support of Pd nanoparticles (PdNPs) in HMF oxidation, their

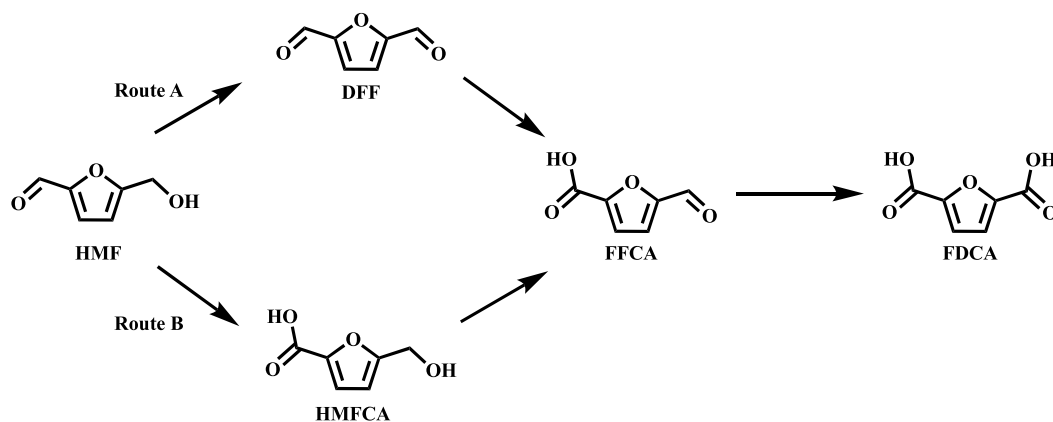**Scheme 1. Possible Reaction Pathways to Produce FDCA from HMF Oxidation**

catalytic properties of bare support materials remain a challenge in this field to reveal the synergistic interactions.[55] In this report, the crucial roles of the intercalation of calcium ion to the MnO_2 framework structures will be highlighted and considered for the capability, ability, and stability in the production of FDCA.[56] Notwithstanding their wide studies, the intercalation of calcium on the structural MnO_2 material used for catalytic reactions of HMF oxidation is a curiosity gap for making significant advances.

To the best of our knowledge, the ambiguous predictive understanding of K^+ and Ca^{2+} cations in the structural manganese dioxides is still worth demonstrating the catalytic activity on aerobic oxidation of HMF due to considerable Mn ions being an active site. In this work, we construct K^+ and Ca^{2+} cations during the formation of manganese oxides in the presence of a KOH solution to improve the unique chemical and physical properties. In addition, the efficient and reusable heterogeneous catalysts of $K-MnO_2$ and $Ca-MnO_2$ on the reactivity of FDCA production will be reported.
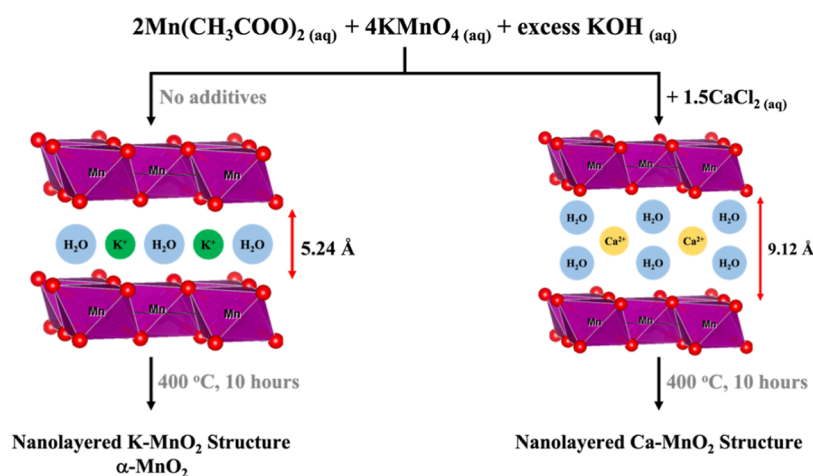
2. EXPERIMENTAL APPARATUS AND METHODOLOGIES

2.1. General. All chemicals and solvents including 5-hydroxymethylfurfural (HMF, Aldrich), 2,5-diformylfuran (DFF, TCI), 5-hydroxymethyl-2-furancarboxylic acid (HMFCA, TCI), 5-formyl-2-furancarboxylic acid (FFCA, TCI), 2,5-furandicarboxylic acid (FDCA, TCI), sodium hydrogen carbonate ($NaHCO_3$, RCI Labscan), sodium carbonate (Na_2CO_3, RCI Labscan), sodium hydroxide (NaOH, RCI Labscan), potassium hydroxide (KOH, Carlo Erba), acetonitrile (CH_3CN, Honeywell), methanol (CH_3OH, Honeywell), potassium chloride (KCl, Carlo Erba), calcium chloride ($CaCl_2$, Unilab), and manganese standard (1000 ppm, Perkin) were of analytical grade and used as received without further purifications. Commercial manganese(IV) oxide (MnO_2, 60−230 mesh, Aldrich) was activated at 300 °C for 10 h before being used for comparison experiments. Deionized water ($R \geq 18.2$ MΩ·cm) was obtained from Nanopure Analytical Deionization Water.

The solid samples revealed the structural orientation by powder X-ray diffraction (XRD), operated by a Bruker D2 Phaser. The X-ray was generated by Cu tube for Cu-K_α radiation at 40 kV and 40 mA and detected by LYNXEYE_XE-T (1D mode). The XRD patterns were recorded with scanning angle (2θ) in the range of 10−90° at 0.2 s/step. The characteristic vibrational frequencies were

carried out by attenuated total reflection Fourier transform infrared (ATR-FTIR) spectroscopy using Bruker Hong Kong Limited model ALPHA. The maximum wavelength (nm) of HMF, DFF, HMFCA, FFCA, and FDCA was investigated by UV−vis spectroscopy (UV-2600 SHIMADZU), operated in the range 200−800 nm. Thermogravimetric analysis (DSC/TGA) was performed using a TA Instruments SDT2960 simultaneously at a heating rate of 10 °C/min up to 800 °C under an air condition. The elemental compositions within the materials were investigated by X-ray photoelectron spectroscopy (XPS) using AXIS ULTRADLD, Kratos Analytical, Manchester, UK. The parameters were used to evacuate in the chamber about 5×10^{-9} Torr and excite with X-ray hybrid mode 700×300 μm spot area using a monochromatic Al Kα 1,2 radiation at 1.4 keV. Transmission electron microscopy (TEM) and energy-dispersive spectroscopy (EDS) was used to characterize the morphology and elemental mapping of the metal ions on manganese oxides accelerating voltage of 200 kV using JEOL (JEM-ARM 200F model), manufactured by JEOL Co., Ltd., Tokyo, Japan. The integrated data acquisition was powered by Digital Micrograph (Gatan Inc., USA) for high-angle annular dark-field imaging (HAADF-STEM) and Analysis Station (JEOL Ltd., Tokyo, Japan) for EDS mapping. N_2 adsorption−desorption isotherms of the solid catalysts were performed on a Nova 2200e model from Quantachrome Instruments, Boynton Beach, FL, USA. Prior to N_2 adsorption, 150 mg of the solid catalysts was outgassed at 300 °C for 3 h under a N_2 flow. Specific surface area, pore volume, and pore diameter were measured by the Brunauer−Emmett−Teller (BET) method. The oxidized products were quantitatively analyzed by high-performance liquid chromatography with a UV−vis detector (HPLC/UV) operating at 283 nm, investigated by UV−vis spectroscopy. The concentrations of HMF and its oxidized derivatives were detected by the WATER e2695 separation module with a UV−vis detector equipped with a Sunfire 5 μm C18 (4.6×150 mm) by using the mixture of acetonitrile and 1% v/v of glacial acetic acid as the mobile phase in the proper proportions. Microwave plasma atomic emission spectroscopy (MP-AES) was used to determine the weight percent (% wt) of K, Ca, and Mn elements in the catalysts using an Agilent 4100 MP-AES.[57]

2.2. Synthesis of K^+ and Ca^{2+} Intercalated Manganese Dioxide ($K-MnO_2$ and $Ca-MnO_2$). The formation of Ca−MnO_2 catalyst was prepared by a developed method by varying the molar ratio of $Ca^{2+}/Mn^{2+}/Mn^{7+}$, as shown in Table S1.[53] The $K-MnO_2$ catalyst was similar to the synthetic procedure

$$2Mn(CH_3COO)_{2\,(aq)} + 4KMnO_{4\,(aq)} + excess\ KOH_{(aq)}$$

No additives

+ 1.5CaCl$_{2\,(aq)}$

5.24 Å

9.12 Å

400 °C, 10 hours

400 °C, 10 hours

Nanolayered K-MnO$_2$ Structure
α-MnO$_2$

Nanolayered Ca-MnO$_2$ Structure

Figure 1. Synthetic procedure of birnessite-type potassium and calcium manganese oxides and the calcined catalysts as well as the proposed structures.
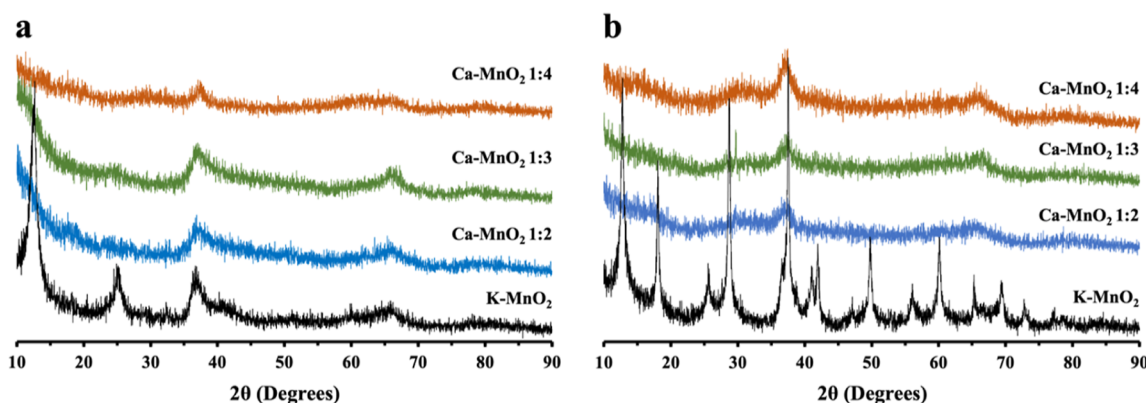
Figure 2. XRD patterns of (a) before and (b) after calcination at 400 °C for 10 h of K−MnO$_2$, Ca−MnO$_2$ 1:2, Ca−MnO$_2$ 1:3, and Ca−MnO$_2$ 1:4.

without CaCl$_2$. Typically, solution **A** was added dropwise into solution **B** and vigorously stirred at room temperature for 1 h to obtain a dark brown suspension. For more information, a mixture of solution **A** was prepared by using KMnO$_4$ (4 mmol, 316 mg) in the presence of KOH (14.20 g) dissolved in DI water (100 cm^3). A mixture of the solution **B** was prepared by using Mn(CH$_3$COO)$_2$ (8 mmol, 1961 mg) and CaCl$_2$ (6, 4, or 3 mmol, respectively) depending on the molar ratio of Ca^{2+} and a total of Mn^{n+} as 1:2, 1:3, or 1:4, respectively in the presence of DI water (10 cm^3). After completing the catalyst synthesis, they were collected by centrifugation at 7500 rpm for 10 min and washed several times with DI water until the pH value of water was approximately 6 to 7. The obtained solids were dried in the oven at 100 °C overnight and then calcined at 400 °C for 10 h.

2.3. Aerobic Oxidation of HMF in the High-Pressure Reactor. FDCA production was successfully studied by reacting in a highly pressurized reactor, as shown in Figure S1. HMF (0.25 mmol, 32 mg, 25 μL) was dissolved in H$_2$O (5 cm^3) and then 1 mol/dm^3 of NaHCO$_3$ (3 equiv). The catalysts were used by calculating the same amount of manganese oxide at 100 mg based on mass % in each element from MP-AES analysis, as shown in Table S2. After that the catalysts of activated commercial MnO$_2$ (100 mg), K−MnO$_2$ (125 mg), or Ca−MnO$_2$ (125 mg) was directly added into the reactor and pressurized with O$_2$ (0.5 MPa). The reactor started the process in a sand bath at 150 °C for 24 h. After completion of the

reaction, the internal solution was quenched by 1 mol/dm^3 of HCl and the solid catalyst separated out by centrifugation at 7500 rpm for 10 min. The crude products were collected and washed by methanol and DI water several times. All collected solutions were adjusted into a volumetric flask size 25 cm^3 and prepared on a small vial to analyze by the HPLC/UV technique.

2.4. Reusability of K−MnO$_2$ and Ca−MnO$_2$ Catalysts. After finishing the reaction, the catalysts were collected by centrifugation at 7500 rpm for 10 min and washed several times with DI water. To completely remove any organic substances that might be adsorbed on the surface of the catalyst, methanol solvent was used to wash the catalyst in the final step and dried in the oven at 100 °C overnight. According to the deactivated catalyst by moisture content, the used catalysts were calcined at 300 °C for 10 h before being used the next time.

3. RESULTS AND DISCUSSION

The easy fabrication of the birnessite structure on the K−MnO$_2$ and Ca−MnO$_2$ by the reaction of Mn(CH$_3$COO)$_2$ and KMnO$_4$ with and without Ca^{2+} addition in the presence of KOH is illustrated in Figure 1 and their crystalline structures were confirmed by XRD patterns, as shown in Figure 2. Alternative building units of nanosized materials were relied on the single-step process to obtain a high yield of self-assembly nanosheets. The XRD patterns of K−MnO$_2$ and Ca−MnO$_2$
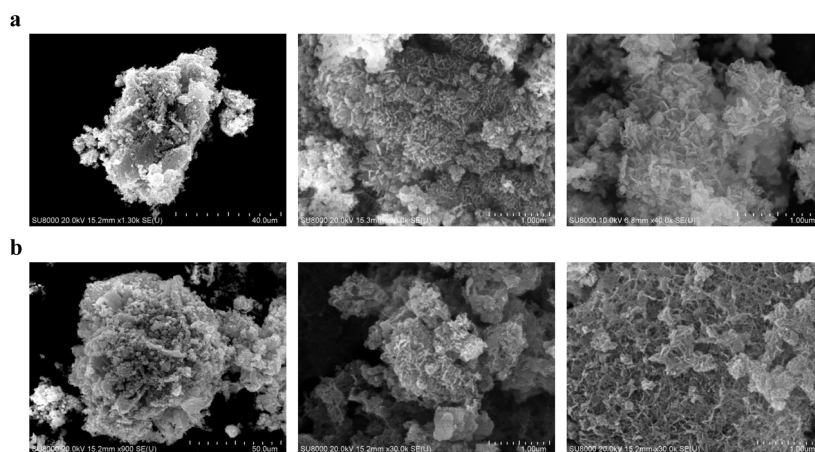
Figure 3. SEM images of (a) K−MnO$_2$ and (b) Ca−MnO$_2$ 1:4 at the difference in magnifications.
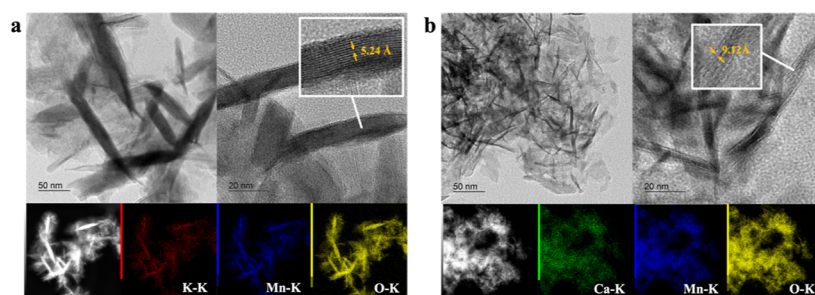

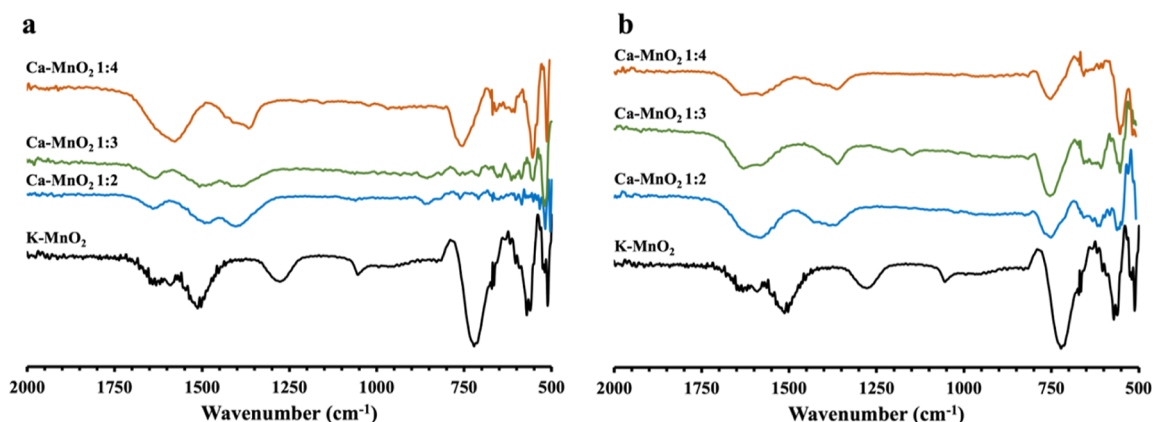**Figure 4.** TEM/EDS images (inset is the HR-TEM image to calculate d-spacing values) of (a) K−MnO$_2$ and (b) Ca−MnO$_2$ 1:4.

Figure 5. ATR-IR spectra of (a) freshly prepared and (b) first used catalysts of K−MnO$_2$, Ca−MnO$_2$ 1:2, Ca−MnO$_2$ 1:3, and Ca−MnO$_2$ 1:4.

before and after calcination at 400 °C for 10 h were summarized in Figure 2a,b. The characteristic XRD patterns of K−MnO$_2$ before calcination appeared at 12.6, 25.4, 37.1, and 66.3°, corresponding to the (001), (002), (100), and (110) miller plane indices, respectively, as shown in Figure 2a. The data were observed in the self-assembled materials of intercalated K$^+$ in the MnO$_2$ materials.[58] The XRD results before calcination of Ca−MnO$_2$ with the ratio difference between Ca^{2+} and the total of Mn^{n+} in Figure 2a showed the poor resolution at 37.6 and 67.1° because of the amorphous character of typical nanolayered calcium−manganese oxides.[54] The crystalline Ca−MnO$_2$ nanoparticles were verified after calcination at 400 °C for 10 h that the structure was calcium-type birnessite, as shown in Figure 2b. Based on the well-established birnessite MnO$_2$, the structural equivalent inter-

stitial site on corner and edge participating MnO$_6$ octahedra could be intercalated by the cation and water into the framework. K$^+$ and Ca^{2+} are commonly reported as the intercalating cations, for which the salt ions were surrounded by water molecules and inserted between the layers. To understand the major hydrous manganese(IV) oxide bearing K$^+$ and Ca^{2+} mineral cations, the composition of H$_2$O was found in the interlayer region that was confirmed by the weight loss (%) of H$_2$O in DSC/TGA analysis, as shown in Figure S2. Interestingly, the effect of thermal decomposition on phase transformation of K−MnO$_2$ was investigated in Figure 2b and formed as the characteristic peaks of α-MnO$_2$ (JCPDS no. 00-044-0141) appear at 12.7, 18.0, 25.7, 28.8, 37.5, 41.9, 49.8, and 60.2°.[50]

SEM images of the synthesized $K-MnO_2$ and $Ca-MnO_2$ 1:4 catalysts are shown in the nanolayered particle morphology in Figure 3a,b, respectively. MnO_2 was intercalated by K^+ and Ca^{2+} ions, showing aggregated nanoparticles with a size of approximately 40−50 μm, which could be observed in more detail at higher magnifications due to the difference in layering. The TEM images of the synthesized catalysts confirmed that the material texture consisted of randomly stacked nanosheets, as shown in Figure 4. The bulkiness of the transmission electron gain showed the opacity of the nanosheet-like pattern in the range of nanometers. The lengths of $K-MnO_2$ and $Ca-MnO_2$ 1:4 were in the ranges of 50−200 and 20−80 nm, respectively. The thicknesses of $K-MnO_2$ and $Ca-MnO_2$ 1:4 were in the ranges of 10−50 and 2−6 nm, respectively. An interatomic spacing for $K-MnO_2$ and $Ca-MnO_2$ 1:4 was defined as the d-spacing value of 5.24 and 9.12 Å, respectively, which affected by cation and water in the layer of MnO_2.[59] The thickness of the transmission electron gain showed the opacity of the tube-like pattern. The elemental determination performed by MP-AES (Figure S3 and Table S2), SEM/EDX (Figure S4), and TEM/EDS (Figure S5) that was an analytical identification of the existence of K^+ and Ca^{2+} into the structural MnO_2 framework.

The specific stretching vibration of symmetric Mn−O band for the chain of MnO_6 oxide was indicated at 560 cm^{-1} that could be considered as a layered manganese oxide, as shown in Figure 5.[54] For $Ca-MnO_2$ 1:2 and $Ca-MnO_2$ 1:3, the strong intensity around 560 cm^{-1} disappeared due to the increased proportion of Ca^{2+}, as shown in Figure 5a. The vibration band in Figure 5b at 750−710 cm^{-1} related to Mn−O−Mn, which was observed in all used catalysts after activation at 300 °C for 10 h. FTIR spectra showed the moisture uptake with a broad band at ∼3500−3200 and 1600 cm^{-1}, corresponding to O−H stretching (antisymmetric and symmetric modes) and H−O−H bending, respectively.

The BET analysis was determined using a multipoint in the P/P_0 range of 0.00−1.00. The specific surface area (m^2/g), pore volume (cc/g), and pore diameter (nm) of activated MnO_2, $K-MnO_2$, and $Ca-MnO_2$ 1:4 showed in Table 1 and

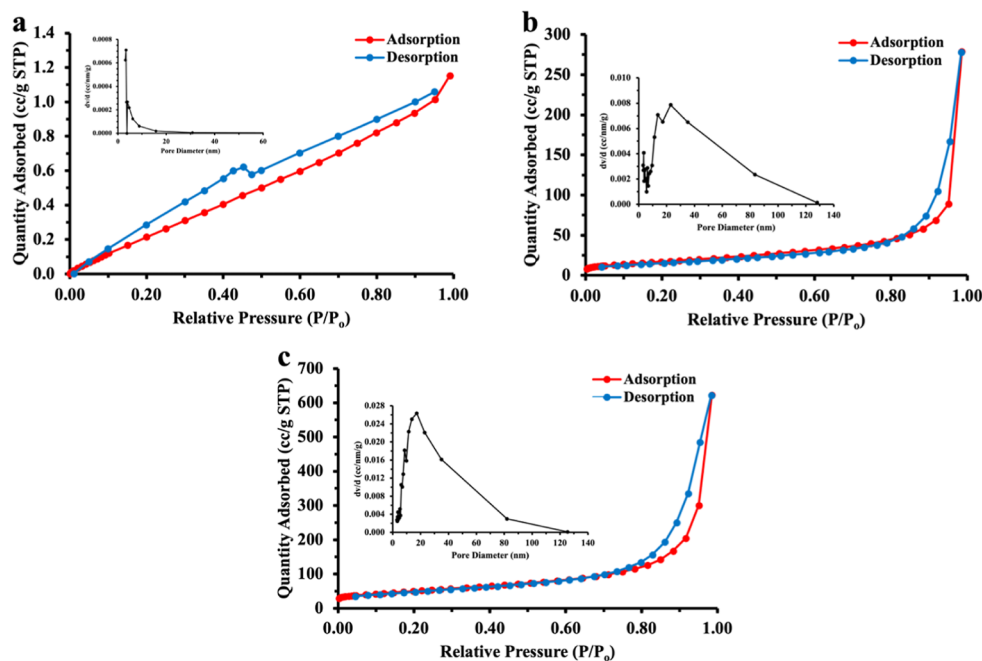**Table 1. BET Analysis for the N_2 Adsorption−Desorption Isotherm and Pore Size Distribution of $K-MnO_2$ and $Ca-MnO_2$ 1:4**

catalysts	specific surface area (m^2/g)	pore volume (cc/g)	pore diameter (nm)
MnO_2	1	0.00163	3.32
$K-MnO_2$	60	0.433	22.91
$Ca-MnO_2$ 1:4	173	0.960	17.20

Figure 6. The specific surface areas of $K-MnO_2$ and $Ca-MnO_2$ 1:4 revealed 160 and 173 m^2/g, respectively. BET surface area measurement presented the results of activated MnO_2 that corresponded to the sieved size of about 60−230 mesh. The nitrogen adsorption−desorption isotherm of $K-MnO_2$ and $Ca-MnO_2$ 1:4 could be regarded as a typical type IV isotherm, indicating the mesoporous nature in structural birnessite.[60]

To investigate the different valence states of manganese oxides derived from the intercalated K^+ and Ca^{2+} cations, the XPS survey spectrum in Table S3 and Figure S6 was analyzed in the regions of K 2p, Ca 2p, Mn 3s, Mn 2p, and O 1s. For K−Mn and Ca−Mn oxides, the Mn 3s core level spectra

demonstrated a spin-energy separation (ΔE) of Mn ions due to the hole−electron exchange of the Mn 3s and the 3d electron in the ground state.[55,61,62] The experimental analysis showed that the exchange splitting values of K−Mn and Ca−Mn oxides were 4.72 and 5.20 eV, respectively, as shown in Figure 7. The region of Mn $2p_{3/2}$ revealed the valence states of +2, +3, and +4 at binding energies of 643.6, 642.4, and 641.2 eV, respectively.[63] The percentage of each oxidation state was calculated by deconvolution, as shown in Table S4. Therefore, the reasonable results based on the magnitude of the 3s exchange splitting and the Mn $2p_{3/2}$ confirmed the mixture of Mn-oxidation states between +3 and +4 in K−Mn and Ca−Mn oxides. The broad O 1s spectra at 530.1, 531.4, and 532.3 eV of K−Mn and Ca−Mn oxides were fitted with components of Mn−O, Mn−O−H, cation (K^+ or Ca^{2+})−OH and adsorbed H−O−H.[63] The binding energies of K $2p_{3/2}$ and K $2p_{1/2}$ in Figure 7a were shown at 292.6 and 295.3 eV, respectively. Moreover, the binding energies of Ca $2p_{3/2}$ and Ca $2p_{1/2}$ in Figure 7b were shown at 347.1 and 350.6 eV, respectively. The XPS analysis in the region of K 2p, Ca 2p, Mn 2p, and O 1s of catalysts after the reaction confirmed the stability of chemical states in each metal element, as shown in Figure S7.

According to the characterization of K−Mn and Ca−Mn oxides, the results from XPS and XRD suggested structural patterns of $K-MnO_2$ and $Ca-MnO_2$ 1:4. From further investigation of calcined $K-MnO_2$ from MP-AES elemental analysis, the existence of nanolayered manganese oxides that contained the distribution of K^+ cation on the structure was confirmed. It was implied that the $K-MnO_2$ catalyst was the mixed component of nanolayered $K-MnO_2$ and α-MnO_2. The effect of the reactivity relationship of K^+ and Ca^{2+} cations on the MnO_2 crystal structure was studied in the aerobic oxidation of HMF into FDCA in the presence of $NaHCO_3$ (3 equiv) as a base under high pressurized oxygen (0.5 MPa) at a high temperature. The oxidized products were investigated by HPLC/UV operating at 283 nm compared to UV−vis spectra, as shown in Figure S8. The catalytic activity and the control experiments used in the comparison are shown in Tables 2 and S5. The results without catalysts in three different conditions showed that FDCA did not occur. Interestingly, the HMF reaction in the absence of $NaHCO_3$ could not be converted to the oxidized products with the low conversion. Humin was easily produced at high temperature in the condition without the catalysts. In addition, the control reactions in Table S5 presented improved performance in the conditions of $NaHCO_3$ and O_2. To investigate the catalytic activity of K−MnO_2 and Ca−MnO_2 with the different Ca/Mn molar ratios of 1:2, 1:3, and 1:4, the commercial MnO_2 was studied (Table 2). The activated MnO_2 showed that the FDCA production values at 150 and 200 °C were 0 and 11%, respectively, where the main oxidized product was FFCA (entries 4 and 9). The K−MnO_2 revealed that the expected FDCA products were 37 and 49% at 150 and 200 °C, respectively. It could be seen that the major product that occurred was FFCA, indicating that the rate-determining step of FFCA to FDCA was the essence of this reaction. Interestingly, the promising Ca−MnO_2 in all proportions showed exceptional results to obtain the FDCA as the majority at 150 °C with 44, 51, and 63% for 1:2, 1:3, and 1:4, as shown in entries 6, 7, and 8, respectively. In addition, the % yield of FDCA was dramatically increased at 200 °C to 75, 81, and 85% for 1:2, 1:3, and 1:4, respectively (entries 11, 12, and 13). Due to the oxidizing agents, which could be either molecular oxygen or $NaHCO_3$, the aerobic oxidation of HMF
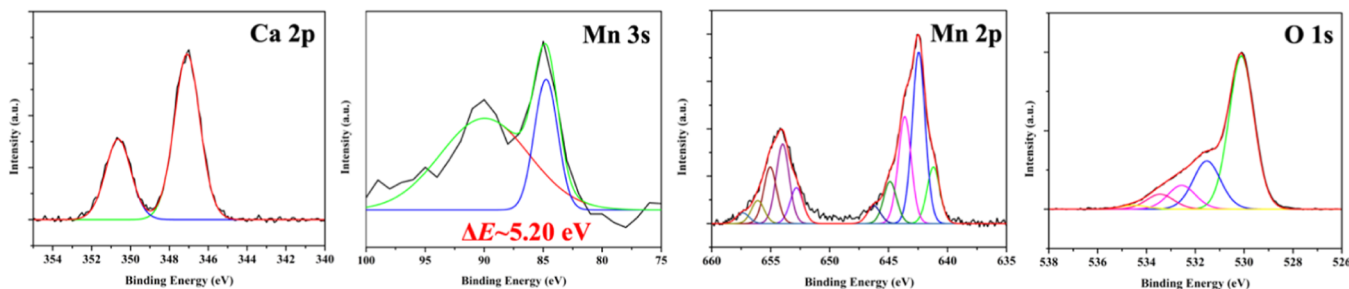
Figure 6. BET analysis for N_2 adsorption−desorption isotherm and pore size distribution of (a) activated MnO_2, (b) $K−MnO_2$, and (c) $Ca−MnO_2$ 1:4.

(a) K-MnO₂
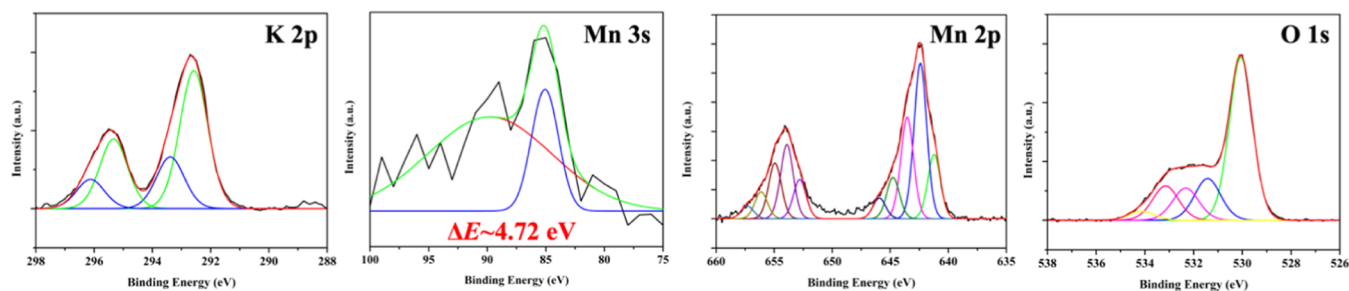
(b) Ca-MnO₂ 1:4

Figure 7. XPS spectra of (a) $K−MnO_2$ and (b) $Ca−MnO_2$ 1:4 before the reaction in the regions of K 2p, Ca 2p, Mn 3s, Mn 2p, and O 1s.

was thoroughly examined, as shown in Table S5. The catalytic performance of $CaMnO_2$ 1:4 was investigated for the ratio of oxygen and $NaHCO_3$ at 200 °C for 24 h. The results showed that $NaHCO_3$ and O_2 played a crucial role in the aerobic oxidation of HMF. Lower concentrations of $NaHCO_3$ and oxygen reduced the efficiency at which the oxidized products was generated. In addition, bases including $NaHCO_3$, Na_2CO_3, and NaOH elucidated the stability of catalysts and the catalytic performance, as shown in Table S6 and Figure S9. The results

showed that $NaHCO_3$ was the most effective and decreased when using the bases of Na_2CO_3 and NaOH, respectively. In addition, the XRD patterns (Figure S9b) of the layered birnessite structure of $Ca−MnO_2$ 1:4 changed after reacting with Na_2CO_3 and NaOH due to the reduced composition of the Ca^{2+} cation into the MnO_2.[64] The stability and selectivity of the $K−MnO_2$ and the $Ca−MnO_2$ 1:4 were considered in reusability at 200 °C under the desired condition, as shown in Figure S10. The $Ca−MnO_2$ 1:4 in the cycling experiment

Table 2. Catalytic Activity of Various Types of Catalysts in HMF Oxidation[a]

entry	catalyst	NaHCO$_3$ (equiv)	O$_2$ (MPa)	air (MPa)	% conv.	% yield			
						HMFCA	DFF	FFCA	FDCA
1	–	3	–	0.1	70	–	20	21	–
2	–	–	0.5	0.1	13	–	–	–	–
3	–	3	0.5	0.1	67	–	22	21	–
4	MnO$_2$[b,d]	3	0.5	0.1	54	–	14	25	–
5	K–MnO$_2$[b]	3	0.5	0.1	100	–	12	40	37
6	Ca–MnO$_2$ 1:2[b]	3	0.5	0.1	100	–	–	37	44
7	Ca–MnO$_2$ 1:3[b]	3	0.5	0.1	100	–	–	29	51
8	Ca–MnO$_2$ 1:4[b]	3	0.5	0.1	100	–	–	23	63
9	MnO$_2$[c,d]	3	0.5	0.1	79	–	21	37	11
10	K–MnO$_2$[c]	3	0.5	0.1	100	–	–	33	49
11	Ca–MnO$_2$ 1:2[c]	3	0.5	0.1	100	–	–	21	75
12	Ca–MnO$_2$ 1:3[b]	3	0.5	0.1	100	–	–	17	81
13	Ca–MnO$_2$ 1:4[c]	3	0.5	0.1	100	–	–	13	85

[a]The percentage of conversion and yield were calculated by a linear regression equation in each standard substance of HMF, HMFCA, DFF, FFCA, and FDCA. [b]**Note:** the HMF oxidation was catalyzed by desired catalysts in the presence of NaHCO$_3$, O$_2$, and air using the temperature outside the reactor of 150 °C. [c]200 °C for 24 h. [d]Purchased MnO$_2$ (60–230 mesh) was activated by thermal treatment at 300 °C for 10 h to remove the moisture of the surface.

showed the ability to produce highly selective FDCA. In addition, the XRD patterns of K–MnO$_2$ and Ca–MnO$_2$ 1:4 before and after the oxidation reaction confirmed the stable of structural MnO$_2$, as shown in Figure S10. In addition, the small quantities for leaching amounts of metal species in the filtrate confirmed the possibility of the heterogeneous nature of K–MnO$_2$ and Ca–MnO$_2$ 1:4, as shown in Table S7. To summarize the reaction pathways, the aerobic oxidation of HMF catalyzed by K–MnO$_2$ and the Ca–MnO$_2$ 1:4 suggested that the reaction occurred via DFF (Route A) because the HMFCA product was not encouraged. The results were consistent with the HMF oxidation of manganese catalysts.[50] In addition, a kinetic study of HMF oxidation was performed to investigate the performance of K–MnO$_2$ and Ca–MnO$_2$ 1:4 by considering the percentage of HMF conversion and FDCA yield, as shown in Figure S11. Unfortunately, the reaction profile of DFF and FFCA was hard to follow due to the heterogeneous system and unstable intermediates. The formation rate of FDCA catalyzed by Ca–MnO$_2$ 1:4 was more effective than that of K–MnO$_2$ over the time course because of the surface area. The catalytic performance of Ca–MnO$_2$ 1:4 was comprehensive compared to the other non-noble metal supported catalyst, as shown in Table S8. The reusability of Ca–MnO$_2$ 1:4 showed a good performance at least 3 times with a slight reduction of FDCA in Figure 8. The possible mechanism of HMF oxidation was proposed to be the reaction on the surface of nanolayered catalysts with the synergistic effect of NaHCO$_3$ and O$_2$, as shown in Figure 9.

4. CONCLUSIONS

The effective catalytic systems of K$^+$ and Ca^{2+} intercalated to the structural MnO$_2$ were clarified to be an active and reusable nonprecious metal oxide toward the aerobic oxidation of HMF to high selective FDCA in the presence of NaHCO$_3$ and O$_2$. The high surface area of the catalysts represented the sole factor affecting the efficiency due to the stable Mn^{3+} and Mn^{4+} active sites on the surface. The K–MnO$_2$ and Ca–MnO$_2$ 1:4 catalysts were stable and able to be reused without a significant loss in the activity. Promising improvements in nanolayer materials provide valuable insights into the further development of biomass-derived precursors.
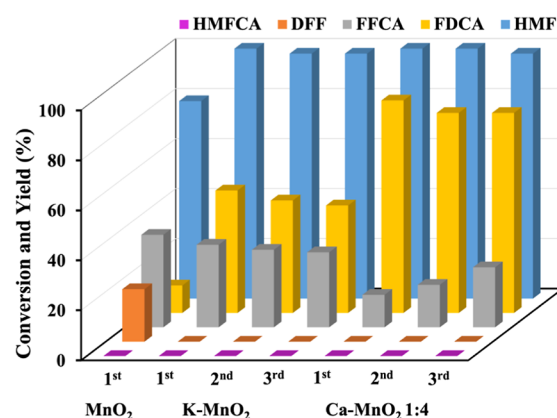

Figure 8. Catalytic activity and reusability at 200 °C of MnO$_2$, K–MnO$_2$, and Ca–MnO$_2$ 1:4.
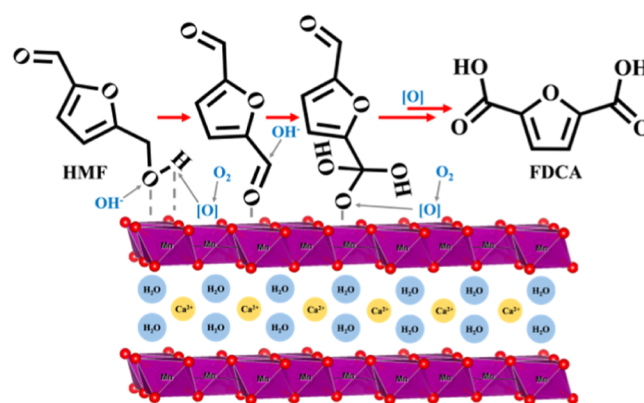

Figure 9. Proposed reaction mechanism on the catalyst surface for the oxidation of HMF to FDCA.

■ ASSOCIATED CONTENT

ⓢ Supporting Information

The Supporting Information is available free of charge at https://pubs.acs.org/doi/10.1021/acsomega.3c06333.

Details about the experimental setup for a batch HMF oxidation; thermograms; calibration curves of Ca, Mn,

and K concentrations; XPS spectra; UV−vis spectra; XRD patterns; kinetic studies; experimental data of the preparation and the catalytic activities; and leaching tests (PDF)

AUTHOR INFORMATION

Corresponding Author

Ekasith Somsook − *NANOCAST Laboratory, Center for Catalysis Science and Technology (CAST), Department of Chemistry and Center of Excellence for Innovation in Chemistry, Faculty of Science, Mahidol University, Bangkok 10400, Thailand;* ⓘ orcid.org/0000-0002-4659-8349; Phone: +66-2-201-5123; Email: ekasith.som@mahidol.ac.th

Authors

Thinnaphat Poonsawat − *NANOCAST Laboratory, Center for Catalysis Science and Technology (CAST), Department of Chemistry and Center of Excellence for Innovation in Chemistry, Faculty of Science, Mahidol University, Bangkok 10400, Thailand*

Peerapong Promcharoen − *NANOCAST Laboratory, Center for Catalysis Science and Technology (CAST), Department of Chemistry and Center of Excellence for Innovation in Chemistry, Faculty of Science, Mahidol University, Bangkok 10400, Thailand*

Titiya Meechai − *Department of Premedical Science, Faculty of Medicine, Bangkokthonburi University, Bangkok 10170, Thailand*

Laksamee Chaicharoenwimolkul Chuaitammakit − *Chemistry and Applied Chemistry, Faculty of Science and Technology, Suratthani Rajabhat University, Surat Thani 84100, Thailand*

Complete contact information is available at:
https://pubs.acs.org/10.1021/acsomega.3c06333

Author Contributions

T.P.: conceptualization, methodology, investigation, validation, visualization, and writing—original draft. P.P.: investigation and recommendation L.C.C.: research design, data analysis, conclusion, recommendation, writing—reviewing and editing, and supervision. T.M.: research design, data analysis, conclusion, recommendation, writing—reviewing and editing, and supervision. E.S.: conventionalization, investigation, writing—original draft, supervision, and project administration.

Notes

The authors declare no competing financial interest.

ACKNOWLEDGMENTS

REFERENCES

(1) Liang, C.; Gracida-Alvarez, U. R.; Hawkins, T. R.; Dunn, J. B. Life-cycle assessment of biochemicals with clear near-term market potential. *ACS Sustainable Chem. Eng.* **2023**, *11* (7), 2773−2783.

(2) Battista, F.; Moustakas, K.; Nizami, A.-S. Integrated biorefinery for the planet's future. *Renewable Energy* **2021**, *170*, 796−799.

(3) Wiranarongkorn, K.; Im-orb, K.; Patcharavorachot, Y.; Maréchal, F.; Arpornwichanop, A. Comparative techno-economic and energy analyses of integrated biorefinery processes of furfural and 5-hydroxymethylfurfural from biomass residue. *Renewable Sustainable Energy Rev.* **2023**, *175*, 113146.

(4) Leong, H. Y.; Chang, C. K.; Khoo, K. S.; Chew, K. W.; Chia, S. R.; Lim, J. W.; Chang, J. S.; Show, P. L. Waste biorefinery towards a sustainable circular bioeconomy: a solution to global issues. *Biotechnol. Biofuels* **2021**, *14* (1), 87.

(5) Chheda, J. N.; Huber, G. W.; Dumesic, J. A. Liquid-phase catalytic processing of biomass-derived oxygenated hydrocarbons to fuels and chemicals. *Angew. Chem., Int. Ed. Engl.* **2007**, *46* (38), 7164−7183.

(6) Maity, S. K. Opportunities, recent trends and challenges of integrated biorefinery: Part I. *Renewable Sustainable Energy Rev.* **2015**, *43*, 1427−1445.

(7) Saidi, M.; Samimi, F.; Karimipourfard, D.; Nimmanwudipong, T.; Gates, B. C.; Rahimpour, M. R. Upgrading of lignin-derived bio-oils by catalytic hydrodeoxygenation. *Energy Environ. Sci.* **2014**, *7* (1), 103−129.

(8) Bozell, J. J.; Petersen, G. R. Technology development for the production of biobased products from biorefinery carbohydrates—the US Department of Energy's "Top 10" revisited. *Green Chem.* **2010**, *12* (4), 539.

(9) Agostinho, B.; Silvestre, A. J. D.; Sousa, A. F. From PEF to rPEF: disclosing the potential of deep eutectic solvents in continuous de-/re-polymerization recycling of biobased polyesters. *Green Chem.* **2022**, *24* (8), 3115−3119.

(10) Fei, X.; Wang, J.; Zhu, J.; Wang, X.; Liu, X. Biobased poly(ethylene 2,5-furancoate): no longer an alternative, but an irreplaceable polyester in the polymer industry. *ACS Sustainable Chem. Eng.* **2020**, *8* (23), 8471−8485.

(11) Hou, Q.; Qi, X.; Zhen, M.; Qian, H.; Nie, Y.; Bai, C.; Zhang, S.; Bai, X.; Ju, M. Biorefinery roadmap based on catalytic production and upgrading 5-hydroxymethylfurfural. *Green Chem.* **2021**, *23* (1), 119−231.

(12) Zhao, Y.; Cai, M.; Xian, J.; Sun, Y.; Li, G. Recent advances in the electrocatalytic synthesis of 2,5-furandicarboxylic acid from 5-(hydroxymethyl)furfural. *J. Mater. Chem. A* **2021**, *9* (36), 20164−20183.

(13) Chen, C.; Wang, L.; Zhu, B.; Zhou, Z.; El-Hout, S. I.; Yang, J.; Zhang, J. 2,5-Furandicarboxylic acid production via catalytic oxidation of 5-hydroxymethylfurfural: catalysts, processes and reaction mechanism. *J. Energy Chem.* **2021**, *54*, 528−554.

(14) Ricciardi, L.; Verboom, W.; Lange, J.-P.; Huskens, J. Production of furans from C5 and C6 sugars in the presence of polar organic solvents. *Sustainable Energy Fuels* **2022**, *6* (1), 11−28.

(15) Zhang, Z.; Deng, K. Recent advances in the catalytic synthesis of 2,5-furandicarboxylic acid and its derivatives. *ACS Catal.* **2015**, *5* (11), 6529−6544.

(16) Deshan, A. D. K.; Atanda, L.; Moghaddam, L.; Rackemann, D. W.; Beltramini, J.; Doherty, W. O. S. Heterogeneous catalytic conversion of sugars into 2,5-furandicarboxylic acid. *Front. Chem.* **2020**, *8*, 659 From NLM PubMed-not-MEDLINE.

(17) Zhang, W.; Qian, H.; Hou, Q.; Ju, M. The functional and synergetic optimization of the thermal-catalytic system for the selective oxidation of 5-hydroxymethylfurfural to 2,5-diformylfuran: a review. *Green Chem.* **2023**, *25* (3), 893−914.

(18) Wang, F.; Yan, C.; Jiang, R.; Chen, Y.; Wei, Y.; Cao, Y.; Guan, W.; Huo, P.; Zhang, Y. Highly efficient aerobic oxidation of 5-hydroxymethylfurfural to 2,5-furandicarboxylic acid over halloysite nanotubes-templated nitrogen-doped carbon supported bimetallic AuPd catalyst. *Appl. Clay Sci.* **2023**, *235*, 106872.

(19) Derflinger, C.; Kamm, B.; Paulik, C.; Meissner, G.; Spod, H. Efficient and selective aerobic oxidation of 5-hydroxymethylfurfural to 2,5-diformylfuran at moderate reaction conditions with design of experiments approach. *ChemistrySelect* 2022, 7 (36), No. e202201211.

(20) Han, X.; Geng, L.; Guo, Y.; Jia, R.; Liu, X.; Zhang, Y.; Wang, Y. Base-free aerobic oxidation of 5-hydroxymethylfurfural to 2,5-furandicarboxylic acid over a Pt/C-O-Mg catalyst. *Green Chem.* 2016, 18 (6), 1597−1604.

(21) Li, Q.; Ma, C. L.; He, Y. C. Effective one-pot chemoenzymatic cascade catalysis of biobased feedstock for synthesizing 2,5-diformylfuran in a sustainable reaction system. *Bioresour. Technol.* 2023, 378, 128965.

(22) Chen, Z.; Wang, Y.; Cheng, H.; Zhou, H. Integrated chemo- and biocatalytic processes: a new fashion toward renewable chemicals production from lignocellulosic biomass. *J. Chem. Technol. Biotechnol.* 2023, 98 (2), 331−345.

(23) Guo, L.; Zhang, X.; Gan, L.; Pan, L.; Shi, C.; Huang, Z. F.; Zhang, X.; Zou, J. J. Advances in selective electrochemical oxidation of 5-hydroxymethylfurfural to produce high-value chemicals. *Adv. Sci.* 2023, 10 (4), No. e2205540.

(24) Lin, Z.; Chen, X.; Lu, L.; Yao, X.; Zhai, C.; Tao, H. Recent advances in electrocatalytic oxidation of 5-hydroxymethylfurfural to 2,5-furandicarboxylic acid: mechanism, catalyst, coupling system. *Nanotechnol. Rev.* 2023, 12 (1), 20220518.

(25) Zhao, D.; Su, T.; Wang, Y.; Varma, R. S.; Len, C. Recent advances in catalytic oxidation of 5-hydroxymethylfurfural. *Mol. Catal.* 2020, 495, 111133.

(26) Neaţu, F.; Marin, R. S.; Florea, M.; Petrea, N.; Pavel, O. D.; Pârvulescu, V. I. Selective oxidation of 5-hydroxymethyl furfural over non-precious metal heterogeneous catalysts. *Appl. Catal., B* 2016, 180, 751−757.

(27) Xia, H.; An, J.; Hong, M.; Xu, S.; Zhang, L.; Zuo, S. Aerobic oxidation of 5-hydroxymethylfurfural to 2,5-difurancarboxylic acid over Pd-Au nanoparticles supported on Mg-Al hydrotalcite. *Catal. Today* 2019, 319, 113−120.

(28) Kar, S.; Zhou, Q. Q.; Ben-David, Y.; Milstein, D. Catalytic furfural/5-hydroxymethyl furfural oxidation to furoic acid/furan-2,5-dicarboxylic acid with H₂ production using alkaline water as the formal oxidant. *J. Am. Chem. Soc.* 2022, 144 (3), 1288−1295.

(29) Messori, A.; Fasolini, A.; Mazzoni, R. Advances in catalytic routes for the homogeneous green conversion of the bio-based platform 5-hydroxymethylfurfural. *ChemSusChem* 2022, 15 (13), No. e202200228.

(30) Qian, H.; Hou, Q.; Zhang, W.; Nie, Y.; Lai, R.; Ren, H.; Yu, G.; Bai, X.; Wang, H.; Ju, M. Construction of electron transport channels and oxygen adsorption sites to modulate reactive oxygen species for photocatalytic selective oxidation of 5-hydroxymethylfurfural to 2,5-diformylfuran. *Appl. Catal., B* 2022, 319, 121907.

(31) Zhu, P.; Zhang, W.; Li, Q.; Xia, H. Visible-light-driven photocatalytic oxidation of 5-hydroxymethylfurfural to 2,5-furandicarboxylic acid over plasmonic Au/ZnO catalyst. *ACS Sustainable Chem. Eng.* 2022, 10 (27), 8778−8787.

(32) Zhang, W.; Li, Q.; Xia, H. Photocatalytic oxidation of 5-hydroxymethylfurfural to furandicarboxylic acid over the Au-Ag/TiO₂ catalysts under visible light irradiation. *Appl. Surf. Sci.* 2023, 613, 156036.

(33) Sailer-Kronlachner, W.; Rosenfeld, C.; Böhmdorfer, S.; Bacher, M.; Konnerth, J.; Rosenau, T.; Potthast, A.; Geyer, A.; van Herwijnen, H. W. G. Scale-up of production of 5-hydroxymethylfurfural-rich adhesive precursors and structural features of humin side products. *Biomass Convers. Biorefin.* 2022.

(34) Megías-Sayago, C.; Lolli, A.; Bonincontro, D.; Penkova, A.; Albonetti, S.; Cavani, F.; Odriozola, J. A.; Ivanova, S. Effect of gold particles size over Au/C catalyst selectivity in HMF oxidation reaction. *ChemCatChem* 2020, 12 (4), 1177−1183.

(35) Kim, M.; Su, Y.; Fukuoka, A.; Hensen, E. J. M.; Nakajima, K. Aerobic oxidation of 5-(hydroxymethyl)furfural cyclic acetal enables selective furan-2,5-dicarboxylic acid formation with CeO₂-supported

gold catalyst. *Angew. Chem., Int. Ed. Engl.* 2018, 57 (27), 8235−8239 From NLM PubMed-not-MEDLINE.

(36) Timofeev, K. L.; Kharlamova, T. S.; Ezhov, D. M.; Salaev, M. A.; Svetlichnyi, V. A.; Vodyankina, O. V. Hydroxymethylfurfural oxidation over unsupported Pd-Au alloy catalysts prepared by pulsed laser ablation: synergistic and compositional effects. *Appl. Catal., A* 2023, 656, 119121.

(37) Salakhum, S.; Prasertsab, A.; Pornsetmetakul, P.; Saenluang, K.; Iadrat, P.; Chareonpanich, M.; Wattanakit, C. Pt nanoparticles on ZSM-5 nanoparticles for base-free oxidation of 5-hydroxymethylfurfural to 2,5-furandicarboxylic acid. *ACS Appl. Nano Mater.* 2021, 4 (12), 14047−14059.

(38) Qi, X.; Zhou, R.; Ai, H.-J.; Wu, X.-F. HMF and furfural: promising platform molecules in rhodium-catalyzed carbonylation reactions for the synthesis of furfuryl esters and tertiary amides. *J. Catal.* 2020, 381, 215−221.

(39) Wang, T.; Song, Y.; Zhao, W.; Zhou, C.; Jin, Y.; Wan, X.; Dai, Y.; Yang, Y. Electro-catalytic oxidation of HMF to FDCA over RuO₂/MnO₂/CNT catalysts in base-free solution. *New J. Chem.* 2021, 45 (45), 21285−21292.

(40) Dibenedetto, A.; Aresta, M.; Pastore, C.; di Bitonto, L.; Angelini, A.; Quaranta, E. Conversion of fructose into 5-HMF: a study on the behaviour of heterogeneous cerium-based catalysts and their stability in aqueous media under mild conditions. *RSC Adv.* 2015, 5 (34), 26941−26948.

(41) Bi, D.; Chen, X.; Du, Z.; Guo, Z.; Liu, Z.; Lin, J.; Huang, Y.; Tang, C.; Chen, G.; Fang, Y. Cobalt supported on BN catalyst with high B-O defects and its efficient hydrodeoxygenation performance of HMF to DMF**. *ChemistrySelect* 2022, 7 (8), No. e202104043.

(42) Taitt, B. J.; Nam, D.-H.; Choi, K.-S. A comparative study of nickel, cobalt, and iron oxyhydroxide anodes for the electrochemical oxidation of 5-hydroxymethylfurfural to 2,5-furandicarboxylic acid. *ACS Catal.* 2019, 9 (1), 660−670.

(43) Ke, Q.; Jin, Y.; Ruan, F.; Ha, M. N.; Li, D.; Cui, P.; Cao, Y.; Wang, H.; Wang, T.; Nguyen, V. N.; et al. Boosting the activity of catalytic oxidation of 5-hydroxymethylfurfural to 2,5-diformylfuran over nitrogen-doped manganese oxide catalysts. *Green Chem.* 2019, 21 (16), 4313−4318.

(44) Yan, H.; Liu, B.; Zhou, X.; Meng, F.; Zhao, M.; Pan, Y.; Li, J.; Wu, Y.; Zhao, H.; Liu, Y.; et al. Enhancing polyol/sugar cascade oxidation to formic acid with defect rich MnO₂ catalysts. *Nat. Commun.* 2023, 14 (1), 4509 From NLM PubMed-not-MEDLINE.

(45) Lokhande, P.; Sonone, K.; Dhepe, P. L. Industry-oriented method for the aqueous phase oxidation of crude 5-hydroxymethyl furfural (HMF) to 2,5-furandicarboxylic acid (FDCA). *New J. Chem.* 2023, 47, 15325−15335.

(46) Ban, H.; Cheng, Y.; Wang, L.; Li, X. One-pot method for the synthesis of 2,5-furandicarboxylic acid from fructose: in situ oxidation of 5-hydroxymethylfurfural and 5-acetoxymethylfurfural over Co/Mn/Br catalysts in acetic acid. *Ind. Eng. Chem. Res.* 2023, 62 (1), 291−301.

(47) Chen, S.; Guo, X.; Ban, H.; Pan, T.; Zheng, L.; Cheng, Y.; Wang, L.; Li, X. Reaction mechanism and kinetics of the liquid-phase oxidation of 5-hydroxymethylfurfural to 2,5-furandicarboxylic acid. *Ind. Eng. Chem. Res.* 2021, 60 (47), 16887−16898.

(48) Chen, S.; Cheng, Y.; Ban, H.; Zhang, Y.; Zheng, L.; Wang, L.; Li, X. Liquid-phase aerobic oxidation of 5-hydroxymethylfurfural to 2,5-furandicarboxylic acid over Co/Mn/Br catalyst. *Ind. Eng. Chem. Res.* 2020, 59 (39), 17076−17084.

(49) Zuo, X.; Chaudhari, A. S.; Snavely, K.; Niu, F.; Zhu, H.; Martin, K. J.; Subramaniam, B. Kinetics of homogeneous 5-hydroxymethyl-furfural oxidation to 2,5-furandicarboxylic acid with Co/Mn/Br catalyst. *AIChE J.* 2017, 63 (1), 162−171.

(50) Hayashi, E.; Yamaguchi, Y.; Kamata, K.; Tsunoda, N.; Kumagai, Y.; Oba, F.; Hara, M. Effect of MnO₂ crystal structure on aerobic oxidation of 5-hydroxymethylfurfural to 2,5-furandicarboxylic acid. *J. Am. Chem. Soc.* 2019, 141 (2), 890−900.

(51) Hayashi, E.; Komanoya, T.; Kamata, K.; Hara, M. Heterogeneously-catalyzed aerobic oxidation of 5-hydroxymethylfur-

fural to 2,5-furandicarboxylic acid with MnO_2. *ChemSusChem* **2017**, *10* (4), 654−658.

(52) Najafpour, M. M.; Ehrenberg, T.; Wiechen, M.; Kurz, P. Calcium manganese(III) oxides ($CaMn_2O_4.xH_2O$) as biomimetic oxygen-evolving catalysts. *Angew. Chem., Int. Ed. Engl.* **2010**, *49* (12), 2233−2237.

(53) Amini, M.; Najafpour, M. M.; Naslhajian, H.; Amini, E.; Farnia, S. M. F. Nanolayered manganese-calcium oxide as an efficient catalyst toward organic sulfide oxidation. *RSC Adv.* **2014**, *4* (21), 10851−10855.

(54) Rong, F.; Zhao, J.; Chen, Z.; Xu, Y.; Zhao, Y.; Yang, Q.; Li, C. Highly active water oxidation on nanostructured biomimetic calcium manganese oxide catalysts. *J. Mater. Chem. A* **2016**, *4* (17), 6585−6594.

(55) Yang, J.; Yu, H.; Wang, Y.; Qi, F.; Liu, H.; Lou, L.-L.; Yu, K.; Zhou, W.; Liu, S. Effect of the oxygen coordination environment of Ca-Mn oxides on the catalytic performance of Pd supported catalysts for aerobic oxidation of 5-hydroxymethyl-2-furfural. *Catal. Sci. Technol.* **2019**, *9* (23), 6659−6668.

(56) Kitchaev, D. A.; Dacek, S. T.; Sun, W.; Ceder, G. Thermodynamics of phase selection in MnO_2 framework structures through alkali intercalation and hydration. *J. Am. Chem. Soc.* **2017**, *139* (7), 2672−2681.

(57) Yang, X. A.; Shi, M. T.; Leng, D.; Zhang, W. B. Fabrication of a porous hydrangea-like $Fe_3O_4@MnO_2$ composite for ultra-trace arsenic preconcentration and determination. *Talanta* **2018**, *189*, 55−64 From NLM PubMed-not-MEDLINE.

(58) Kai, K.; Yoshida, Y.; Kageyama, H.; Saito, G.; Ishigaki, T.; Furukawa, Y.; Kawamata, J. Room-temperature synthesis of manganese oxide monosheets. *J. Am. Chem. Soc.* **2008**, *130*, 15938−15943.

(59) Xie, Q.; Cheng, G.; Xue, T.; Huang, L.; Chen, S.; Sun, Y.; Sun, M.; Wang, H.; Yu, L. Alkali ions pre-intercalation of δ-MnO_2 nanosheets for high-capacity and stable Zn-ion battery. *Mater. Today Energy* **2022**, *24*, 100934.

(60) Bao, Y.; Jin, J.; Ma, M.; Li, M.; Li, F. Ion exchange conversion of Na-birnessite to Mg-buserite for enhanced and preferential Cu^{2+} removal via hybrid capacitive deionization. *ACS Appl. Mater. Interfaces* **2022**, *14* (41), 46646−46656 From NLM PubMed-not-MEDLINE.

(61) Koleva, V.; Boyadzhieva, T.; Zhecheva, E.; Nihtianova, D.; Simova, S.; Tyuliev, G.; Stoyanova, R. Precursor-based methods for low-temperature synthesis of defectless $NaMnPO_4$ with an olivine- and maricite-type structure. *CrystEngComm* **2013**, *15* (44), 9080.

(62) Ilton, E. S.; Post, J. E.; Heaney, P. J.; Ling, F. T.; Kerisit, S. N. XPS determination of Mn oxidation states in Mn (hydr)oxides. *Appl. Surf. Sci.* **2016**, *366*, 475−485.

(63) Barai, H. R.; Banerjee, A. N.; Joo, S. W. Improved electrochemical properties of highly porous amorphous manganese oxide nanoparticles with crystalline edges for superior supercapacitors. *J. Ind. Eng. Chem.* **2017**, *56*, 212−224.

(64) Brousse, T.; Toupin, M.; Dugas, R.; Athouël, L.; Crosnier, O.; Bélanger, D. Crystalline MnO_2 as possible alternatives to amorphous compounds in electrochemical supercapacitors. *J. Electrochem. Soc.* **2006**, *153* (12), A2171.